HHS Public Access

Author manuscript

ACS Photonics. Author manuscript; available in PMC 2022 May 19.

Published in final edited form as:

ACS Photonics. 2021 May 19; 8(5): 1430–1438. doi:10.1021/acsphotonics.1c00160.

Bridging the“Last Millimeter” Gap of Brain-Machine Interfaces via Near-Infrared Wireless Power Transfer and Data Communications

Eunseong Moon[†], **Michael Barrow**[†], **Jongyup Lim**[†], **Jungho Lee**[†], **Samuel R. Nason**[‡], **Joseph Costello**[‡], **Hun Seok Kim**[†], **Cynthia Chestek**[‡], **Taekwang Jang**[¶], **David Blaauw**[†], **Jamie D. Phillips**[†,§]

[†]Department of Electrical Engineering and Computer Science, University of Michigan, Ann Arbor, MI USA [‡]Department of Biomedical Engineering, University of Michigan, Ann Arbor, MI USA [¶]Department of Information Technology and Electrical Engineering, ETH Zürich, Zürich, Switzerland [§]Department of Electrical and Computer Engineering, University of Delaware, Newark, DE 19716, USA

Abstract

Arrays of floating neural sensors with high channel count that cover an area of square centimeters and larger would be transformative for neural engineering and brain-machine interfaces. Meeting the power and wireless data communications requirements within the size constraints for each neural sensor has been elusive due to the need to incorporate sensing, computing, communications, and power functionality in a package of approximately 100 micrometers on a side. In this work, we demonstrate a near infrared optical power and data communication link for a neural recording system that satisfies size requirements to achieve dense arrays and power requirements to prevent tissue heating. The optical link is demonstrated using an integrated optoelectronic device consisting of a tandem photovoltaic cell and microscale light emitting diode. End-to-end functionality of a wireless neural link within system constraints is demonstrated using a pre-recorded neural signal between a self-powered CMOS integrated circuit and single photon avalanche photodiode.

Graphical Abstract

jphilli@udel.edu .

Supporting Information Available

Epitaxial layer information, data describing PV/μLED electrical device isolation, and Monte Carlo optical simulations are available in supplementary information.

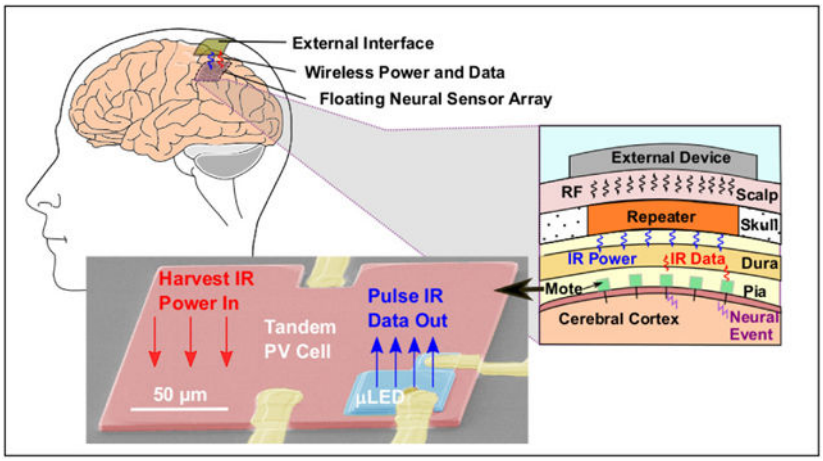

Keywords

optoelectronic devices; photovoltaics; light emitting diodes; wireless sensors; neural engineering

Introduction

Miniature, wireless, injectable neural recording modules that do minimal damage to the brain[1–5] have been a long-standing goal since the early days of neural engineering. Neural recording at the scale of 1,000 or more channels over a several square centimeters has the potential to significantly advance neuroscience and brain machine interfaces. Wired neural probe arrays such as the Utah Array[6,7] are the current state of the art for multi-channel neural recording, but are limited by the routing and tethering forces of the wire bundle, including tethering forces that can cause micro-motion and cause sensors to dislodge over time. A wireless system approach is depicted in Fig. 1a, consisting of a large-area, dense array of neural sensors (often called neural motes or neural dust) that can receive power from, and communicate data to, a larger transplanted skull replacement unit (repeater). The repeater unit may then couple outside the body using an inductively coupled radio-frequency link or direct wired connection. Analogous to the last kilometer/mile problem in transportation and telecommunications, there is a fundamental challenge[8] in bridging the "last millimeter" between the neural motes and the repeater to achieve wireless power and data transfer that meets the complex demands for sensing, computation, and communications of the system.

Implantable neural sensors at the millimeter-scale and sub millimeter-scale have been demonstrated, using the wireless power transfer and data telemetry based on radio-frequency (RF)[4,5] and ultra-sound[1–3] approaches. However, the small size required for neural sensor arrays, and constraints placed by surrounding biological tissue, make these wireless approaches impractical. RF links provide the opportunity to enable high channel count (> 1,000 motes),[5] but suffers from dramatic antenna efficiency loss (> 30 dB) for wireless power transfer[3–5] when scaled to sub-mm size[9] due to lateral and angular misalignments and weak coupling[10] with mm-scale antenna receivers. To boost the efficiency of wireless power transfer, high frequency (> 50 GHz) is required, which results in high tissue absorption and

high power consumption.[11,12] Ultrasound offers a path to high efficiency wireless power transfer[1–3,8,13] comparable to RF approaches, but faces difficulty in scaling to sub-millimeter dimensions due to requirements for bulky transducers and inability for compact vertical integration with CMOS circuitry to enable dense sensor arrays. Near-Infrared light (NIR, 780 – 1700 nm) offers a transparency window for biological tissue[14,15] and optoelectronic device technologies that can offer high efficiency at the micrometer scale. Prior NIR systems for neural recording,[16,17] and for microscopic sensors[18] have been demonstrated, though these systems utilize highly localized laser irradiance of more than 100 mW/mm^2 that exceeds acceptable power levels for large area illumination to ensure that tissue is not damaged due to heating. In this work, we demonstrate wireless NIR power and data communications via an integrated optoelectronic device with a photovoltaic (PV) cell and microscale light emitting diode (μLED) connected to a self-powered CMOS integrated circuit (IC) that meets size and power requirements[8,19] for dense arrays of neural sensors. We demonstrate the working principle of the NIR power and data link using separate optoelectronic and CMOS IC devices (shown in Fig. 1b), which provide size requirements for later heterogeneous integration and packaging into neural motes.

Experimental

To estimate the increase in neural tissue temperature when irradiated, we delivered flood illumination through a craniotomy in a feline ex vivo. After turning a craniotomy and durotomy approximately 1 cm × 1 cm in size, we placed an implantable micro temperature probe[20,21] on the pia surface and covered it with the dura. Then, we delivered 850 nm light for approximately 18 minutes via an array of LEDs through a 3× magnification lens displaced less than 3 cm from the dura and centered above the craniotomy. Following this illumination period, we read out the recorded temperature sampled at a conversion time of 30 ms.

Epitaxial structures for an integrated phototovoltaic (PV) energy harvester and microscale LED (μLED) were designed with details provided in Supporting Information (Table S1). Materials were grown commercially by Visual Photonics Epitaxy, Co (VPEC, Taiwan). We fabricated the PV/μLED modules using conventional fabrication processes, where the chlorine based reactive-ion etching (RIE) process (Cl_2:BCl_3:Ar = 20:20:20 sccm, etch rate : 200 Å/s) to etch down to the desired epitaxial layers both for PV and LED contact layers by controlling the etch depth using the DEKTAK surface profiler, e-beam physical vapor deposition (PVD) of thin metal films using Ti/Pt/Au (50/100/200 nm) for p-type GaAs and Ni/Ge/Au/Ti/Pt/Au (5/30/100/50/100/200 nm) for n-type GaAs, the chemical treatment on the exposed surface and sidewall using the ammonium sulfide (23%) solution for 3 min, plasma enhanced chemical vapor deposition (PECVD) of 300 nm silicon nitride at 350 °C for passivation of the exposed sidewall and anti-reflection coating at 850 nm wavelength were used.

The electrical characteristics of PV/μLED modules under dark and illumination conditions were measured using Keithley 2400 and 4200 parameter analyzers. The calibrated illumination sources including the fiber coupled LED from Thorlabs (M850F2) and 48 LED arrays from CMVision (IRS48) for the emission of 850 nm wavelength were used to

characterize the PV cells. The external quantum efficiency of fabricated LEDs was measured using a calibrated photodetector from Thorlabs (PM120D). End-to-end functionality experiments of the NIR link used a fiber coupled laser source from QPhotonics (QFLD-850–200S) to modulate NIR light to the PV cell and interconnected CMOS IC through a fiber optic reflection y-probe from Thorlabs (RP20). The LED pulsed output for the NIR uplink was detected by a NIR SPAD from AUREA (SPD OEM NIR) through the fiber optic reflection y-probe output.

The CMOS IC used in these experiments was fabricated in 180 nm CMOS technology, and is the second generation of the circuit reported previously.[19] In the end-to-end functionality experiment, the PV/μLED module and the CMOS IC were wire bonded together on a 64-PGA installed on a custom designed printed circuit board. A pre-recorded neural signal was streamed from a Keysight 33600A Trueform Waveform Generator into the input pins of the CMOS IC through a 1000:1 on-PCB signal attenuator. All of the monitoring signals including pre-recorded neural signal, SPAD output signal, and CMOS IC internal signals are monitored via a Saleae Pro 16-ch Logic Analyzer.

Replayed neural data was collected from a nonhuman primate implanted with a 96 channel Utah microelectrode array in the hand area of primary motor cortex. Details of the implantation procedure and experimental setup were described previously.[22] Briefly, we trained an adult male nonhuman primate to perform a one-dimensional task requiring him to move his virtual fingers into a virtual target by moving his physical fingers. While performing this task, we synchronously recorded neural data filtered between 0.3 Hz to 7.5 kHz sampled at 30 kSps. Using a Keysight 33600A Trueform Waveform Generator, we replayed an arbitrary section of one channel's recording to validate end-to-end functionality. The particular channel used included neural action potentials greater than 400 μV in peak-to-peak voltage at an average 53.8 Hz spiking rate.

NIR Transmittance and Power Constraints

The primary power constraint for operation is to limit NIR irradiation to levels that avoid damage from tissue heating, approximately 1–2 °C[23] corresponding to a maximum exposure limit of 1.36 mW/mm^2 from American National Standards Institute (ANSI).[24] Independently, we performed ex vivo experiments post-mortem on a feline using implanted micro temperature probes[20,21] beneath the dura and found a similar exposure limit of approximately 0.8 mW/mm^2 at 850 nm over a 20 minute duration for a uniformly illuminated area of approximate 1 cm in diameter (Fig. 2a). The 20 minute duration was chosen due to the observation that tissue temperature clearly reaches a steady state value, where there is not expected to be an issue with further heat accumulation for continuous NIR irradiation. In a final clinical system, a person with paralysis may want to use the system all the time while awake, so 16 to 24 hours of continuous usage should be accommodated. The somewhat lower limit for NIR exposure that we observed in our experiments relative to the ANSI guidelines may be explained by the absence of blood flow in cerebral tissue and cerebrospinal fluid during the experiments, which carries away heat by perfusion. To ensure we are safely below exposure limits, we select a maximum NIR irradiation limit of 0.64 mW/mm^2 onto the dura which is $<$50% of the ANSI limit. Separate studies on multiphoton

imaging microscopy[16,17] indicated a significantly higher exposure limit on the order of 100 mW/mm^2,[25] though we believe that these studies are not appropriate to inform limits for our proposed neural recording system since they utilized a small beam size rastered over a much smaller 1 mm^2 area. Such high power densities are impractical for under continuous illumination over larger area (> 1 cm^2) to power arrays of 100s to 1,000s of motes. The upper limit that we define for NIR power density corresponds to the maximum recommended temperature increase for tissue, where reduced NIR power density will correspond to reduced tissue heating, but more stringent power and energy requirements on the system.

The power density available at each mote is determined by the transmittance of NIR through the dura. We measured transmittance spectra post-craniotomy on a feline and a non-human primate, where the dura shows high optical transmittance of > 85% for the thinner feline dura and > 35% for the thicker non-human primate at 850 nm (Fig. 2b), which agrees with previously reported transmittance above 30% for human dura in the 700–900 nm wavelength range.[14,15] Assuming a value of 30% for the transmittance for human dura, a maximum NIR optical power delivery of approximately 190 μW/mm^2 is available for an NIR downlink to power neural motes. Requirements for the NIR uplink for data communications between the array of motes and the repeater unit are set by the μLED power available at the mote, the detection limit at the repeater, and the optical path loss between the μled and the repeater. While the NIR power downlink can use flood irradiation over the array of neural sensors, the data uplink will rely on spatially localized NIR pulses at each mote to be detected at the pixel level of the repeater detector array. The simulated optical path loss for an μLED with a Lambertian optical output is shown in Fig. 2c, accounting for tissue absorption and scattering.[15] The simulation is based on the Monte Carlo technique as described in Supporting Information. The efficiency of this optical link is estimated to be η_{dura} = 0.1% for a receiver area of 1×10^4 μm^2. The high NIR transparency and predominant forward scattering for the dura results in an optical link that closely resembles the configuration for a free-space LiFi network[26] where the optical power collected at the receiver is

$$H_{DC} = \frac{(m+1)A_r}{2\pi D^2} cos^m(\phi) cos(\psi) 1_{\psi \le \psi_{FOV}}(\psi) \quad (1)$$

$$m = -log_2(cos(\phi_{1/2})) \quad (2)$$

where ϕ is the radiant angle between source and detector, ψ is the angle between the detector normal and the source, ψ_{FOV} is the detector field of view, A_r is the detector area, D is the source-to-detector distance, and m is the Lambertian emission order determined by the half-power semi-angle $\phi_1/2$. Eq. (1) is a simplified expression for small solid angles of emission (i.e. $D^2 >> A_r$). In addition, we need to consider the possibility of additional optical link losses due to lateral misalignment between a given mote and detector location at the receiver. For a lateral misalignment of 1 mm, optical power will drop by 28% (−1.1 dB) compared to direct alignment, which is small in comparison to the vertical optical path loss in the system. Optical scattering also reduces misalignment loss by diffusing the emitted light. The repeater unit can use high sensitivity detectors such as a single photon avalanche

photodiode (SPAD), where only a few photons at the receiver are needed to trigger a response. The detection limit is determined by the dark count rate of the SPAD, where the number of photons emitted by the μLED (N_{LED}) should exceed

$$N_{LED} > \frac{(DCR)(F)(\Delta t)}{\eta_{dura}\eta_{SPAD}} \quad (3)$$

where η_{dura} is the efficiency of the optical data uplink, η_{SPAD} is the detection efficiency of the SPAD, DCR is the SPAD dark count rate, F is the noise margin (multiplier) for number of photons above DCR desired to achieve the desired signal-to-noise ratio, and Δt is the time window for detection. Assuming conservative values typical of commercial SPAD,[27,28] η_{SPAD} =10%, DCR = 1,000 counts/second; a noise margin of F = 10 (common requirement of 10 dB); and η_{dura} = 0.1%; the μLED is required to provide $N_{LED} > 1\times10^5$ photons for a time window of Δt = 1 ms for 1 kHz detection frequency. This number of photons gives an approximate rule of thumb that the NIR μLED packet energy should be greater than 20 fJ, or optical power that is in the microwatt range for pulse widths in the nanosecond range.

Integrated PV/μLED Module

The critical optical component to enable the NIR power and data communication link is the integrated PV and μLED device for each mote. In this work, we have designed and fabricated a GaAs-based PV and μLED module with characteristics shown in Fig. 3a and b. The device is designed for a power downlink at 850 nm for the PV cell and 1000 nm NIR uplink for data communication. We selected the shorter wavelength (850 nm) for power generation to maximize PV power and voltage generation to the CMOS circuitry. In turn, the longer wavelength for the data communication uplink (1000 nm) reduces the minimum required voltage to drive the μLEDs. The wavelength for the data uplink can ultimately be optimized according to power budget of the mote and performance of detector arrays at the repeater unit, noting that CMOS SPADs[28] may ultimately offer higher performance with the tradeoff requirement of shorter wavelength μLEDs. The size and power requirements for the motes presents challenges including the generation of sufficient voltage from the PV cell, achieving high μLED efficiency at relatively low injection levels, providing adequate μLED light extraction in a small form factor, electrical isolation between the PV and μLED devices, and the minimization of non-radiative losses associated with the exposed perimeters of the device. Our PV cell is based on our previous vertically-stacked dual junction devices[29] that provides double the voltage output of a single junction cell (> 1.4 V) that is sufficient for direct powering of CMOS circuitry without the need for additional voltage boosting circuitry or additional series circuit interconnections of multiple PV cells. The μLED uses an $In_{0.2}Ga_{0.8}As$ multi quantum-well (QW) structure with doping profiles that are optimized to achieve high internal radiative efficiency at low current levels[30,31] and lateral current spreading to improve light extraction efficiency for small layer thickness. To prevent PV cell degradation while μLEDs are forward biased, AlGaAs junction barrier layers are incorporated in the epitaxial structure to achieve electrical isolation, based on a strategy we have used previously for monolithic PV arrays.[32] The full epitaxial structure for the PV/μLED device and data related to device operation are provided in Supporting Information (Table S1 and Figs. S1–S3). The device fabrication process incorporates a series of chemical

surface treatments using ammonium hydroxide and ammonium sulfide[33,34] and thin film passivation to minimize non-radiative losses at the device perimeter.[35] The DC electrical and optical characteristics of the 190 μm × 204 μm PV/μLED device are shown in Fig. 3c–e. The PV cell under 850 nm NIR μLED illumination at 150 μW/mm^2 (below the 190 μW/mm^2 exposure limit set above) demonstrates power conversion efficiency greater than 25 % and provides approximately 1.5 μW at a voltage of 1.35 V (1.6 V open circuit voltage and > 1.1 μA short-circuit current). This power generation is sufficient to directly support miniaturized CMOS control circuitry[19] at illumination levels below the thermal limit described above. The μLED shows exponential I-V characteristics with a turn-on voltage around 1.2 V, which is below the output voltage of the PV cell (Fig. 3d). The optical power output of the μLED is in the nW to 100's of μW range (Fig. 3e), and certainly above our established μLED output power requirement to exceed the detection limit of the system. In order to provide sufficient optical power for detection at the repeater, the μLED driver circuit stacks three capacitors charged directly by the PV cell to drive the μLED with short pulses of higher current (approximately 1 mA) to take advantage of higher μLED efficiency in this range and higher instantaneous light flux to increase detection probability at the receiver.

Self-Powered NIR Neural Link

We demonstrate completely wireless, end-to-end operation of a NIR power and data link using a side-by-side test of the PV/μLED module and CMOS IC as shown in Fig. 4a. The experimental measurement setup mimics the conditions of the link between the mote and receiver using a fiber optic Y-probe for simultaneous 850 nm irradiation of the PV cell for power delivery and NIR collection from the 1000 nm μLED for data communication. During testing, we limited the incident light to 150 μW/mm^2 (below the 190 μW/mm^2 limit set above). The PV cell provides 1.5 μW at a voltage of 1.35 V, where the mote integrated CMOS IC requires continuous power of 0.73 μW in a voltage range from 0.9 – 1.5 V during device operation.[19] This provides a 50 % margin to account for nonidealities and guarantee the perpetual mote operation. Measurements on our fiber optic link setup results in the following link efficiency (power loss) components: 2.9 % (−15.4 dB) for free space path loss between μLED and fiber optic probe, 17 % (−7.7 dB) in the fiber optic link, and 1.5 % (−18.2 dB) for losses between the fiber-optic probe to the SPAD optical coupling (primarily due to mismatch on the fiber input of our SPAD instrument). The total losses of our experimental optical link are therefore estimated at −41.3 dB, which is more lossy than the expected optical uplink (η_{dura} = 0.1 %, −30 dB). Optical pulses with various pulse widths and amplitude are generated by a waveform generator and PV/μLED device for the NIR data up link. As shown in Fig. 4b, pulses generated with 40 μs width and 1.26 V amplitude (corresponding μLED current 839 μA) demonstrate detection at the SPAD with a 10 μs dead time. Furthermore, we examined the detection rate for a series of 300 pulses for a range of μLED pulse width and peak current to examine the threshold to ensure high detection probability. A charge of approximately 20 pC is found to ensure near >99% detection rate (Fig. 4c). The shorter pulses with pulse width at 8 ns and higher μLED applied voltage of 1.57 V (current ~ 3 mA) demonstrates successful detection while offering high energy efficiency through operation in the regime where the μLED offers high quantum efficiency.

Practical neural recording may be accomplished using the approach of spiking band power (SBP),[36–38] with signal amplitude in the 300–1000 Hz band in 10–50 ms windows. The CMOS IC consists of an amplifier chain for neural signal acquisition, an on-chip feature extraction unit, a μLED driver for NIR optical data uplink, and an optical receiver followed by clock and data recovery for NIR optical data downlink. The IC consumes sub-μW of total power that may be fully supplied by the PV cell under NIR illumination at 850 nm and 150μW/mm^2. The dual junction structure of the PV cell allows the CMOS IC to draw supply voltage and current directly from the PV cell without an internal voltage converter. Once the 850 nm NIR light is turned on, the boot-up block of the CMOS IC wakes the system up. When NIR light is modulated between high and low light intensity level, the optical receiver of the CMOS IC fetches the modulated light level into a data 1 or 0. By modulating the NIR light with the constant target frequency or with the pulse width modulation, the CMOS IC recovers its on-chip clock frequency to the target frequency or download configuration data into a register bank, respectively. After the clock and data recovery, the nominal operation of the IC is maintained with constant NIR irradiation. The amplifier chain is composed of a low noise amplifier followed by two variable gain amplifiers and achieves $<10\ \mu V_{rms}$ of input referred noise with >65 dB of the peak gain. The low and high pass corner of the amplifier chain is set by the recovered on-chip clock frequency supporting spiking band power (SBP). The SBP extraction unit integrates the absolute amplitude of the output signal of the amplifier chain in time domain on the chip. Once the integrated value exceeds the programmed threshold, it enables the μLED driver, triggers a μLED pulse train, and resets the integrated value; encoding the measured SBP in the time interval of the adjacent μLED pulse trains. This time-interval-encoded method can significantly reduce the uplink communication bandwidth from the mote to the repeater below to 100s of Hz, but still maintaining relatively accurate motor prediction accuracy.[19] Each μLED pulse train is composed of total 17 pulses where the 10 bits of the unique chip ID[39] and 6 bits of the analog front end gain configuration are encoded in the 16 pulse intervals. A matched filter is used to decode the original data by convolution of the SPAD output with a known set of possible μLED pulse train patterns to generate a final score. The matched filter would ultimately be implemented on the repeater unit in the final system.

The NIR optical link using a pre-recorded neural signal is shown in Fig. 4d. The voltage signal is streamed into the CMOS IC using an arbitrary waveform generator and 1000:1 attenuator on the PCB. The μLED trigger signal in the second row of Fig. 4d, which is the internal signal of the CMOS IC that drives the μLED at its rising edge, is directly monitored through the logic analyzer to compare with the measured SPAD output and decoded event. The CMOS IC computes SBP (absolute average of the input neural signal amplitude in the 300–1000Hz band) and encodes it in the time interval of the adjacent μLED pulse trains such that the time interval is inversely proportional to the SBP. The μLED pulse trains have short time intervals when there is active neural activity, and large time intervals when there is sparse neural activity. For example, the high neural activity region observed near time of 1.2 ms in the top row of Fig. 4d results in a high value of SBP that triggers a μLED pulse with a short time delay between pulses. Conversely, the sparse neural activity near time of 1.4 ms in the top row of Fig. 4d results in a low value of SBP with a long time interval between μLED firing events. This shows that the CMOS IC successfully encodes the

measured SBP in the time interval of the μLED pulse trains as described in the CMOS IC operation. SPAD output on the third row of Fig. 4d is measured through the wireless optical setup detecting 1000 nm light pulse fired by the μLED that is driven by the self-powered CMOS IC. Matched filtered output on the fourth row is generated by correlating the measured SPAD output with the known 16-bit pulse train patterns of the unique chip ID and configuration setup. Local peaks of the matched filtered output represent decoded μLED events. Overall, the wirelessly measured and decoded μLED firing events match to the CMOS IC internal μLED trigger signals validating the proposed NIR link.

Conclusion and Future Implementation

The side-by-side PV/μLED and CMOS chip experiment demonstrates that the key "last millimeter" power and data communication gap may be bridged using near-infrared links. While this work demonstrates the fundamental operating principles, substantial work remains in implementing neural motes and the repeater unit system. To realize the neural motes, the optical layer of the PV//μLED and the CMOS IC may be vertically stacked via heterogeneous integration,[40,41] as shown schematically in Fig. 5. The optical layer and CMOS IC may be thinned to approximately 50 μm each, electrically interconnected by through-wafer vias, and hybridized using solder bump bonding. Motes will ultimately require bio-compatible packaging, for which there are a number of established options. A recommended approach for these motes is to use NIR transparent polymeric epoxy underfill and encapsulation followed by a layer of silicone. This approach has been demonstrated for and LED based cochlear implant in rodents.[42] Following successful mote assembly and packaging, the first experiments will be planned for rats, with a move to monkeys for the purpose of informing a human clinical system. The long-term goal is to increase the channel count for neural recording beyond what is currently available for human use in the Utah array, which cannot safely exceed 384 channels per person. Ultimately, we believe that NIR optical links provide a key enabling technology for wireless power and data transfer that will enable floating neural recording arrays to cover large area and high channel count.

Supplementary Material

Refer to Web version on PubMed Central for supplementary material.

Acknowledgement

This work was supported by the National Institutes of Health under Award under Award R21EY02945201. SRN was supported by NIH grant F31HD098804.

The authors thank Prof. Tim Bruns at the University of Michigan for assistance and laboratory use for the post-craniotomy feline experiments.

References

(1). Seo D; Carmena JM; Rabaey JM; Maharbiz MM; Alon E Model validation of untethered, ultrasonic neural dust motes for cortical recording. J. Neurosci Methods 2015, 244, 114–122. [PubMed: 25109901]

(2). Seo D; Neely R; Shen K; Singhal U; Alon E; Rabaey JM; Carmena JM; Maharbiz MM Wireless recording in the peripheral nervous system with ultrasonic neural dust. Neuron 2016, 91, 529–539. [PubMed: 27497221]

(3). Piech DK; Johnson BC; Shen K; Ghanbari MM; Li KY; Neely RM; Kay JE; Carmena JM; Maharbiz MM; Muller R A wireless millimetre-scale implantable neural stimulator with ultrasonically powered bidirectional communication. Nature Biomed. Eng 2020, 4, 207–222.

(4). Lee J; Laiwalla F; Jeong J; Kilfoyle C; Larson L; Nurmikko A; Li S; Yu S; Leung VW Wireless power and data link for ensembles of sub-mm scale implantable sensors near 1GHz. 2018 IEEE Biomedical Circuits and Systems Conference (BioCAS). 2018; pp 1–4. [PubMed: 29780971]

(5). Lee. J; Leung V; Lee AH; Huang J; Asbeck P; Mercier PP; Shellhammer S; Larson L; Laiwalla F; Nurmikko A Wireless ensembles of sub-mm microimplants communicating as a network near 1 GHz in a neural application. bioRxiv 2020,

(6). Jones KE; Campbell PK; Normann RA A glass/silicon composite intracortical electrode array. Annals of Biomedical Engineering 1992, 20, 423–437. [PubMed: 1510294]

(7). Nordhausen CT; Maynard EM; Normann RA Single unit recording capabilities of a 100 microelectrode array. Brain Research 1996, 726, 129–140. [PubMed: 8836553]

(8). Yang KW; Oh K; Ha S Challenges in scaling down of free-floating implantable neural interfaces to millimeter scale. IEEE Access 2020, 8, 133295–133320.

(9). Rabaey JM; Mark M; Chen D; Sutardja C; Tang C; Gowda S; Wagner M; Werthimer D Powering and communicating with mm-size implants. 2011 Design, Automation & Test in Europe. Grenoble, France, 2011; pp 1–6.

(10). Ho JS; Kim S; Poon AS Midfield wireless powering for implantable systems. Proc. IEEE 2013, 101, 1369–1378.

(11). Poon AS; O'Driscoll S; Meng TH Optimal frequency for wireless power transmission into dispersive tissue. IEEE Trans. Antennas Propag 2010, 58, 1739–1750.

(12). Diaz RE; Sebastian T Electromagnetic limits to radiofrequency (RF) neuronal telemetry. Sci. Rep 2013, 3, 3535. [PubMed: 24346503]

(13). Charthad J; Weber MJ; Chang TC; Arbabian A A mm-sized implantable medical device (IMD) with ultrasonic power transfer and a hybrid bi-directional data link. IEEE J. Solid-State Circuits 2015, 50, 1741–1753.

(14). Eggert HR; Blazek V Optical properties of human brain tissue, meninges, and brain tumors in the spectral range of 200 to 900 nm. Neurosurgery 1987, 21, 459–464. [PubMed: 3683777]

(15). Genina EA; Bashkatov AN; Kochubey VI; Tuchin VV Optical clearing of human dura mater. Opt. Spectrosc 2005, 98, 470–476.

(16). Lee S; Cortese AJ; Trexel P; Agger ER; McEuen PL; Molnar ACA 330m×90m opto-electronically integrated wireless system-on-chip for recording of neural activities. IEEE International Solid-State Circuits Conference (ISSCC). San Francisco, CA, 2018; pp 292–294.

(17). Lee S; Cortese AJ; Gandhi AP; Agger ER; McEuen PL; Molnar ACA 250μm × 57 μm microscale opto-electronically transduced electrodes (MOTEs) for neural recording. IEEE Trans. Biomed. Circuits Syst 2018, 12, 1256–1266. [PubMed: 30334768]

(18). Cortese AJ; Smart CL; Wang T; Reynolds MF; Norris SL; Ji Y; Lee S; Mok A; Wu C; Xia F; Ellis NI; Molnar AC; Xu C; McEuen PL Microscopic sensors using optical wireless integrated circuits. Proc. Natl. Acad. Sci. U S A 2020, 117, 9173–9179.

(19). Lim J; Moon E; Barrow M; Nason SR; Patel PR; Patil PG; Oh S; Kim HS; Sylvester D; Blaauw D; Chestek CA; Phillips JD; Jang TA 0.19×0.17mm2 wireless neural recording IC for motor prediction with near-infrared-based power and data telemetry. 2020 IEEE International Solid-State Circuits Conference. San Francisco, CA, 2020; pp 416–418.

(20). Lee I; Kim G; Moon E; Jeong S; Kim D; Phillips J; Blaauw DA 179-Lux energy-autonomous fully-encapsulated 17-mm 3 sensor node with initial charge delay circuit for battery protection. 2018 IEEE Symposium on VLSI Circuits. 2018; pp 251–252.

(21). Yang K; Dong Q; Jung W; Zhang Y; Choi M; Blaauw D; Sylvester D 9.2 A 0.6 nJ 0.22/+ 0.19 C inaccuracy temperature sensor using exponential subthreshold oscillation dependence. 2017 IEEE International Solid-State Circuits Conference (ISSCC). San Francisco, CA, 2017; pp 160–161.

(22). Irwin ZT; Schroeder KE; Vu PP; Bullard AJ; Tat DM; Nu CS; Vaskov A; Nason SR; Thompson DE; Bentley JN; Patil PG; Chestek CA Neural control of finger movement via intracortical brain–machine interface. J. Neural Eng 2017, 14, 066004. [PubMed: 28722685]

(23). Wolf PD (BMI) In: Reichert WM, editor. Indwelling Neural Implants: Strategies for Contending with the In Vivo Environment. Boca Raton (FL): CRC Press/Taylor & Francis; 2008. Chapter 3. Available from: https://www.ncbi.nlm.nih.gov/books/NBK3932/.

(24). ANSI14 (LIo, America. American National Standard for Safe Use of Lasers (ANSI Z136. 1). Laser Institute of America, Orlando, Florida (2014).

(25). Podgorski K; Ranganathan G Brain heating induced by near-infrared lasers during multiphoton microscopy. J. Neurophysiol 2016, 116, 1012–1023. [PubMed: 27281749]

(26). Haas H; Chen C; O'Brien D A guide to wireless networking by light. Prog. Quantum Electron 2017, 55, 88–111.

(27). Bronzi D; Villa F; Tisa S; Tosi A; Zappa F; Durini D; Weyers S; Brockherde W 100 000 Frames/s 64 × 32 single-photon detector array for 2-D imaging and 3-D ranging. IEEE J. Sel. Topics Quantum Electron 2014, 20, 354–363.

(28). AUREA Technologies - Compact NIR Single Photon Detector Dual-mode photon counting solution - OEM design [900 nm - 1700 nm].

(29). Moon E; Barrow M; Lim J; Blaauw D; Phillips JD Dual-junction GaAs photovoltaics for low irradiance wireless power transfer in submillimeter-scale sensor nodes. IEEE J. Photovolt 2020, 10, 1721–1726. [PubMed: 33224555]

(30). Heikkilä O; Oksanen J; Tulkki J Ultimate limit and temperature dependency of light-emitting diode efficiency. J. Appl. Phys 2009, 105.

(31). Niemeyer M; Kleinschmidt P; Walker AW; Mundt LE; Timm C; Lang R; Hannappel T; Lackner D Measurement of the non-radiative minority recombination lifetime and the effective radiative recombination coefficient in GaAs. AIP Adv. 2019, 9.

(32). Moon E; Lee I; Blaauw D; Phillips JD High-efficiency photovoltaic modules on a chip for millimeter-scale energy harvesting. Prog. Photovolt 2018, 27, 540–546.

(33). Remashan K; Bhat KN Combined effect of (NH4) 2Sx treatment and post-metallization annealing with plasma-enhanced chemical vapour deposition silicon nitride gate dielectric on the GaAs metal-insulator-semiconductor characteristics and the photoluminescence characteristics of GaAs substrates. Semicond. Sci. Technol 2002, 17.

(34). Xuan Y; Lin H-C; Ye P Simplified Surface Preparation for GaAs Passivation Using Atomic Layer-Deposited High-k Dielectrics. IEEE Trans. Electron. Devices 2007, 54, 1811–1817.

(35). Moon E; Blaauw D; Philips JD Infrared energy harvesting in millimeter-scale gaas photovoltaics. IEEE Trans. Electron. Devices 2017, 64, 4554–4560. [PubMed: 29129936]

(36). Stark E; Abeles M Predicting movement from multiunit activity. J. Neurosci 2007, 27, 8387–8394. [PubMed: 17670985]

(37). Irwin ZT; Thompson DE; Schroeder KE; Tat DM; Hassani A; Bullard AJ; Woo SL; Urbanchek MG; Sachs AJ; Cederna PS; Stacey WC; Patil PG; Chestek CA Enabling low-power, multi-modal neural interfaces through a common, low-bandwidth feature space. IEEE Transactions on Neural Systems and Rehabilitation Engineering. 2015.

(38). Nason SR; Vaskov A; Willsey MS; Welle EJ; An H; Vu PP; Bullard AJ; Nu CS; Kao JC; Shenoy KV; Jang T; Kim HS; Blaauw D; Patil PG; Chestek CA A low-power band of neuronal spiking activity dominated by local single units improves the performance of brain-machine interface performance. Nat. Biomed. Eng 2020, 4, 973–983. [PubMed: 32719512]

(39). Yang K; Dong Q; Blaauw D; Sylvester D 8.3 A 553F22-transistor amplifier-based Physically Unclonable Function (PUF) with 1.67% native instability. 2017 IEEE International Solid-State Circuits Conference (ISSCC). San Francisco, CA, 2017; pp 146–147.

(40). Elsherbini AA; Liff SM; Swan JM Heterogeneous integration using omnidirectional interconnect packaging. 2019 IEEE International Electron Devices Meeting (IEDM). San Francisco, CA, 2019.

(41). Ingerly DB et al. Foveros: 3D integration and the use of face-to-face chip stacking for logic devices. 2019 IEEE International Electron Devices Meeting (IEDM). San Francisco, CA, 2019.

(42). Keppeler D et al. Multichannel optogenetic stimulation of the auditory pathway using microfabricated LED cochlear implants in rodents. Science Translational Medicine 2020, 12, eabb8086. [PubMed: 32718992]

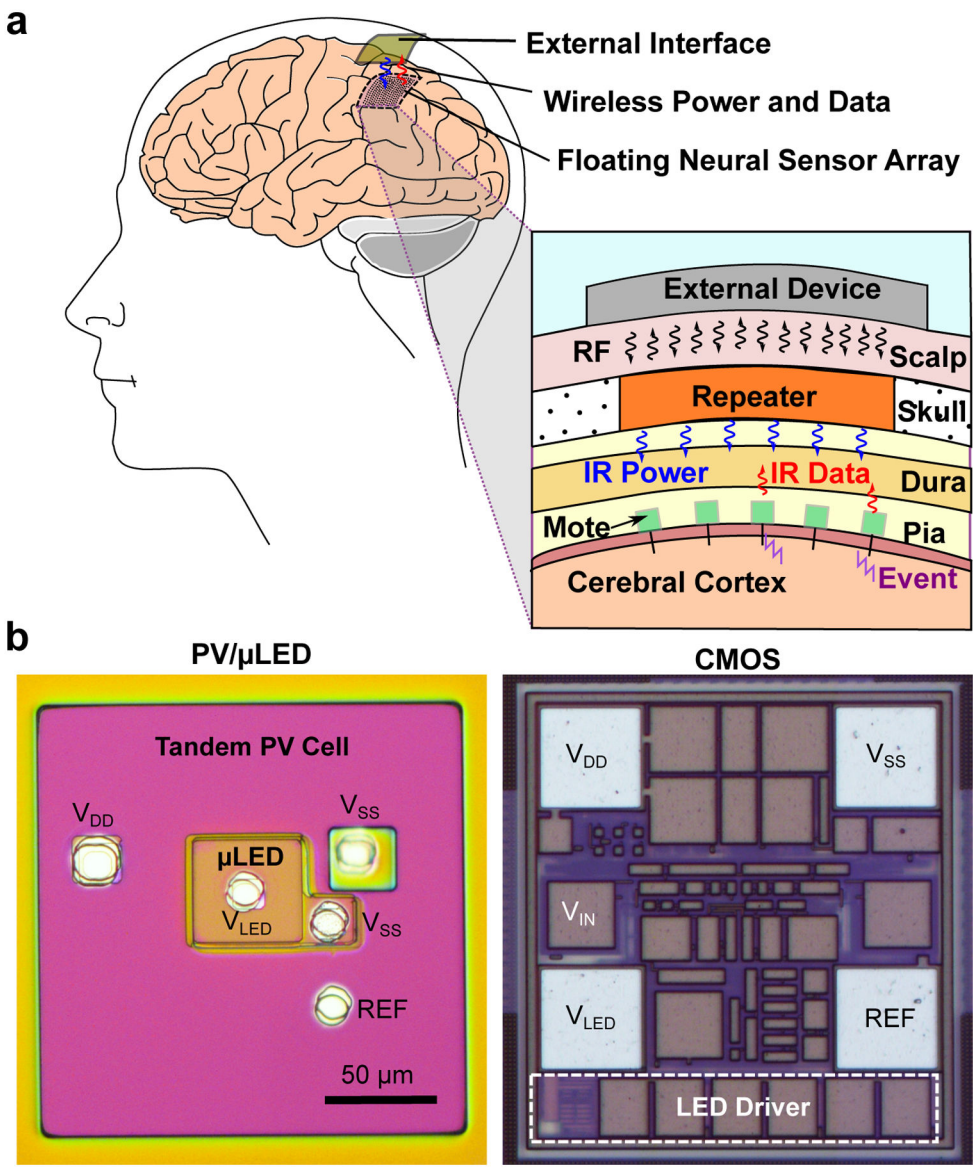

Figure 1:

Conceptual illustration of (a) full system for recording and transmitting the neural signals and (b) optical microscope images of PV/μLED module and CMOS IC used in this work to demonstrate the operating principle for a self-powered mote with NIR wireless power and data transfer.

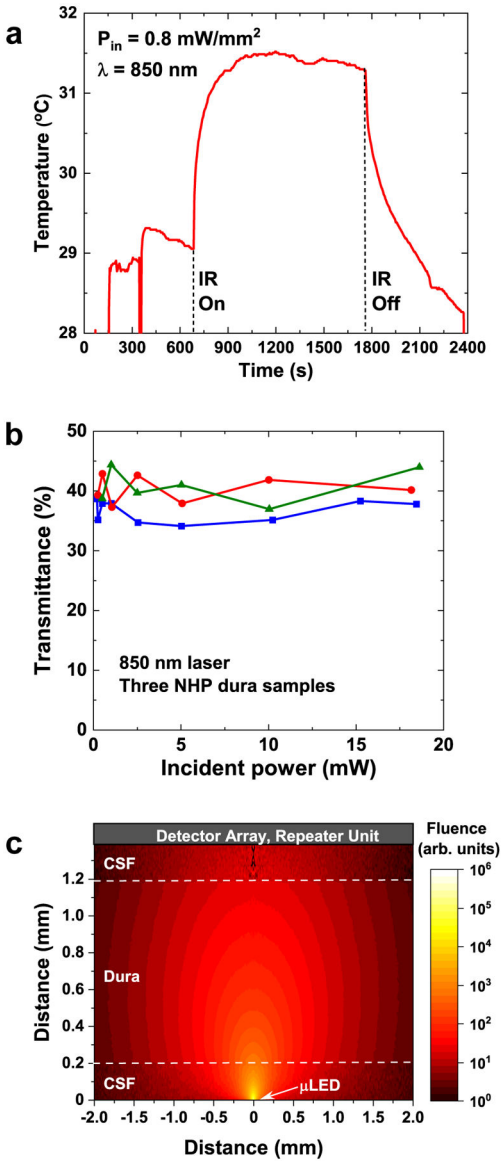

Figure 2:

(a) Measured temperature of post-craniotomy subdural feline brain tissue under 850 nm NIR irradiation over 20 min exposure. (b) Measured NIR transmittance through post-craniotomy NHP dura samples under 850 nm laser illumination. (c) Monte-Carlo simulation of NIR emission from a μLED through dura to the SPAD repeater, with estimated efficiency of 0.1% (photons received at SPAD with 100 μm diameter relative to photons emitted from μLED).

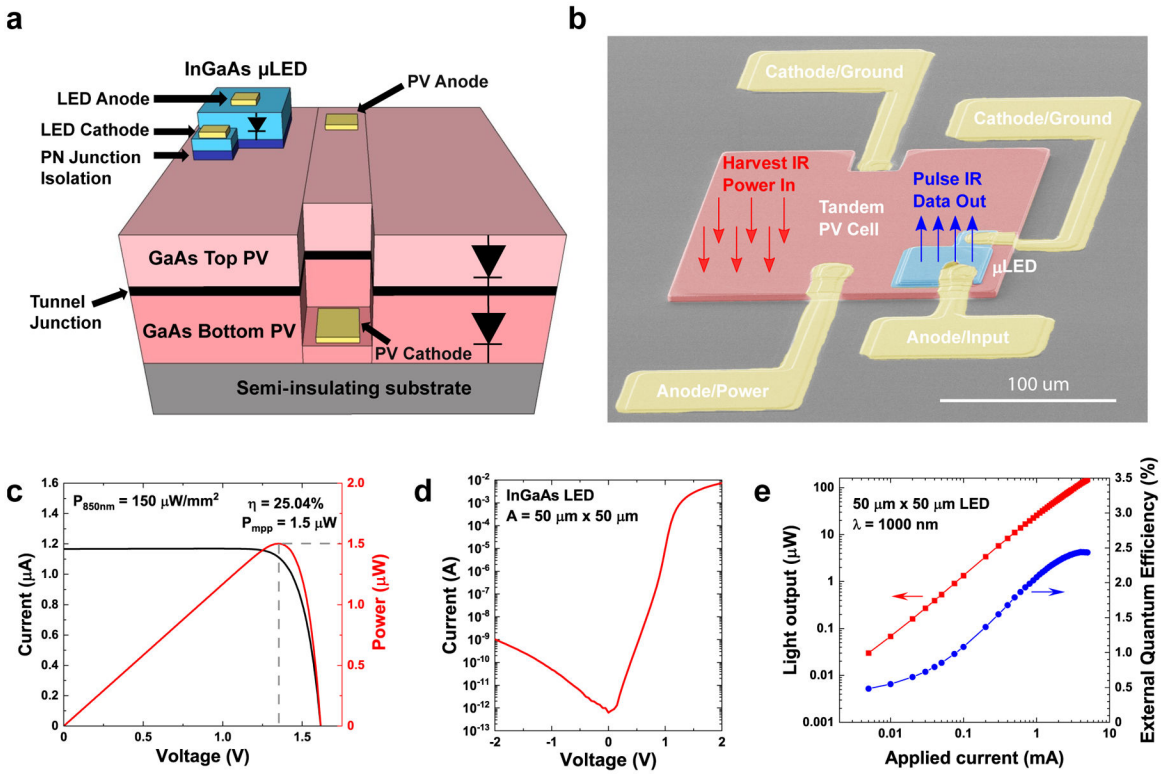

Figure 3:

(a) Schematic diagram of monolithically integrated PV/μLED module illustrating tandem junction of PVs and junction barrier isolation between μLED and PV devices. (b) A scanning electron microscope (SEM) image of a fabricated PV/μLED with included electrical probing pads. (c) Measured I-V and P-V characteristics of dual junction PV cell under 850 nm NIR LED illumination at 100 μW/mm^2. (d) Measured I-V characteristic of fabricated μLED under dark conditions. (e) Measured light output and corresponding external quantum efficiency (EQE) versus applied current of fabricated μLED.

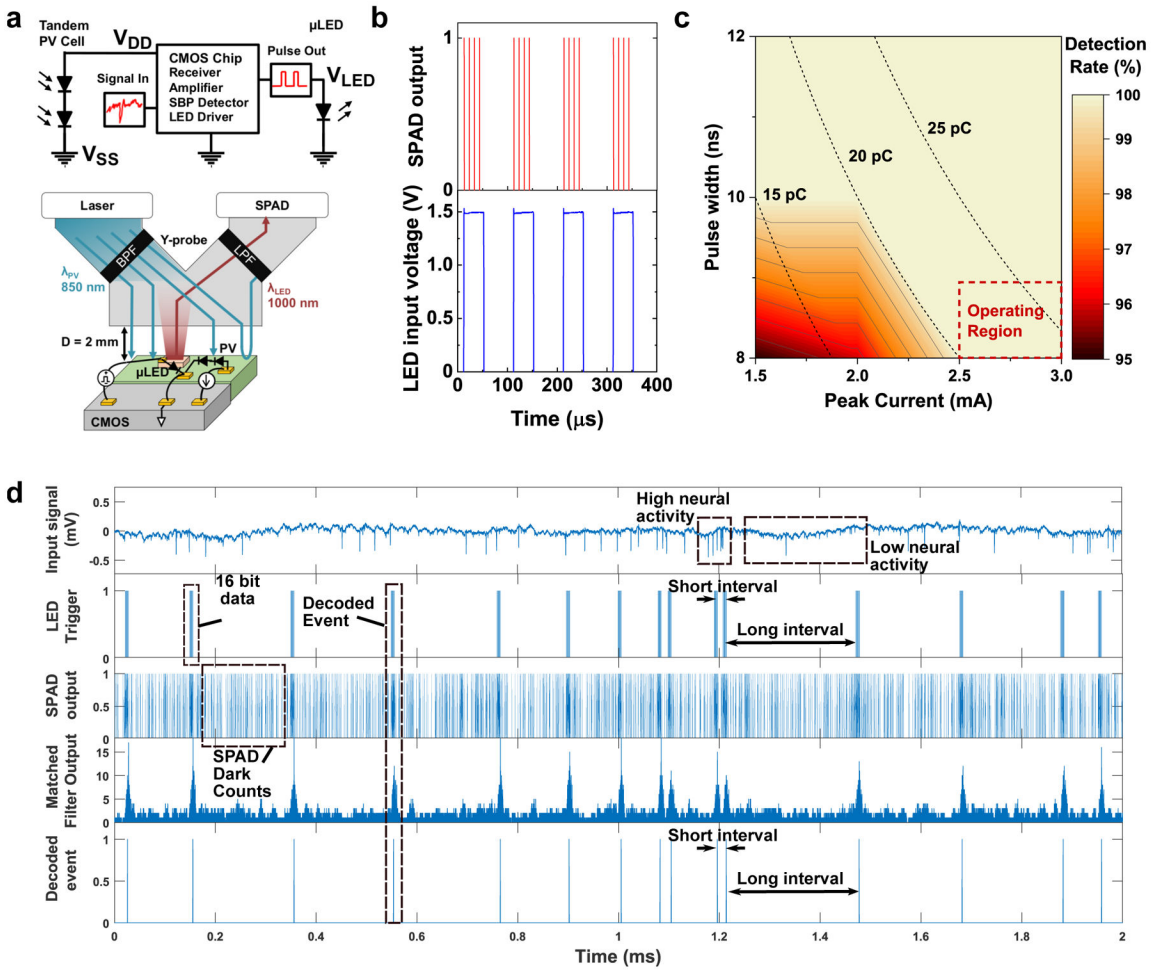

Figure 4:

(a) Optical testing setup using the fiber optic y-probe to demonstrate autonomous and wireless power and data communications and equivalent circuit diagram for PV/μLED module and its connection to CMOS control circuitry. (b) Detected SPAD output (10 μs deadtime) versus LED input pulses (40 μs pulse width, 100 μs period, 1.54 applied voltage). (c) Measured detection rate of SPAD along with μLED pulses with variable applied peak current, pulse width and corresponding charge streamed into μLED (dashed). (d) Demonstration of End-to-end functionality from input neural signal to decode events.

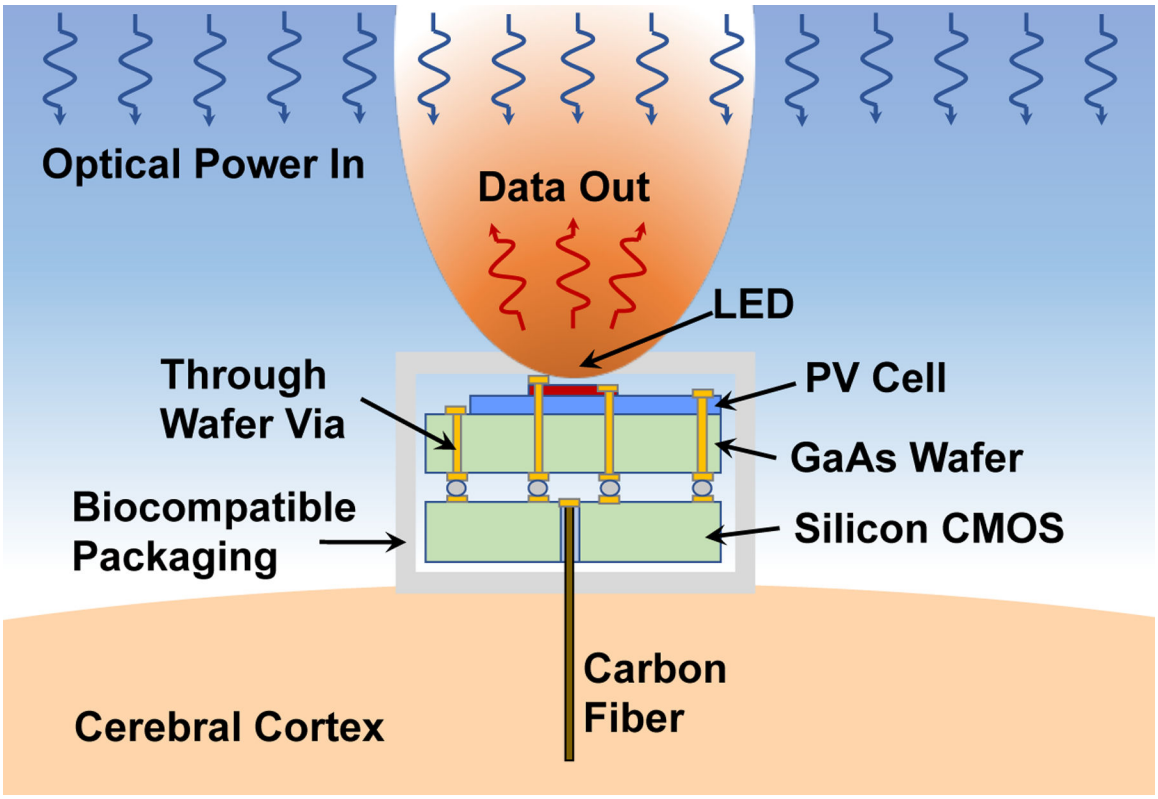

Figure 5:
Conceptual drawing of heterogeneous integration and packaging of a neural mote consisting of a vertically stacked optical layer and CMOS layer and use of carbon fiber probe for sensor input.